Controlling Coupling of Guided to Radiating Modes Using Adiabatic Transitions Between Waveguides of Different Curvature

Yoav Berlatzky, Itay Shtrichman, Romanas Narevich, Edvardas Narevicius, Gershon Rosenblum, and Ilya Vorobeichik

***Abstract*—A simple method for designing adiabatic transitions between straight and curved waveguides is presented. This method results in lower coupling from guided to radiating modes than conventional methods based on introducing an abrupt offset at the junction point. With the new adiabatic transition design, a decrease of 5 to 10 dB in the low-level radiating light cone is found compared with the traditional method.**

***Index Terms*—Integrated optics, optical losses, optical planar waveguides, waveguide bends.**

I. Introduction

INTEGRATED optical circuits almost always require bent waveguide (WG) sections. Introduction of curved WGs increases loss to the cladding (radiating) modes by two main mechanisms: pure bending loss of the curved section itself and transition loss at the junction of two WGs of different curvature. The most frequent case is between a WG of constant radius (arc) and a straight section [1].

A common method for minimizing loss at curved-to-straight WG junctions is by using lateral offsets [2]. Another method is based on using an adiabatic transition, where the curvature smoothly changes from the curvature of the first WG to the curvature of the second WG [3]–[5].

In addition to the insertion loss incurred by bent WG sections and their transitions, each source of loss can also be regarded as a coupler between the WG's guided modes and the stray light in the cladding modes. When viewed as such a coupler, the transition loss mechanism is highly localized compared with the pure bending loss, which is spread over the entire bent section. Some of the excited cladding modes are actually leaky (resonant) modes of the straight WG sections that have long "lifetimes" (decay length) and therefore retain their amplitude for large propagation distances [6]. These leaky modes have important practical implications. First, they can impede the measurement of weak signals due to high background radiation, and second, they can generate coherent interference effects.

The results presented in Fig. 1 demonstrate the said phenomenon. In this experiment, light is coupled into an arc WG of radius $R = 5000$ μm followed by a straight section, where the arc and straight WG are connected with no offset. Fig. 1 shows the light intensity distribution cross section for two distances

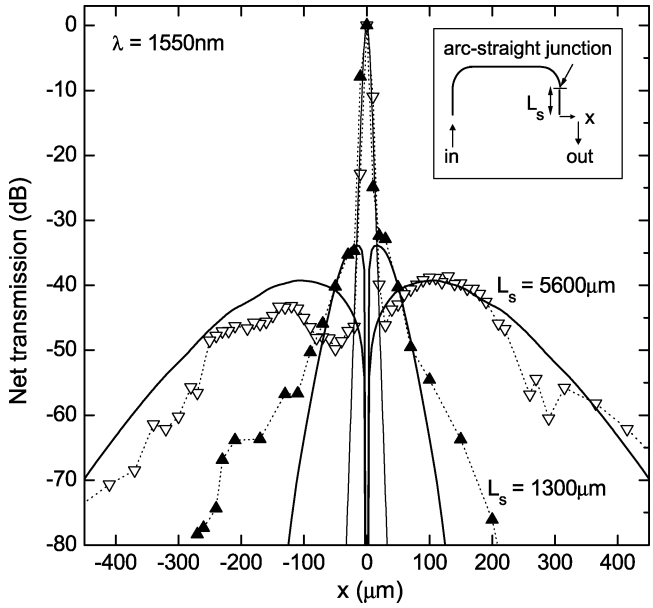

Fig. 1. Light intensity distribution cross sections after an arc-to-straight WG junction. Light propagates in an arc of 5000-μm radius followed by a straight single-mode WG of length L_s (inset). Symbols indicate output light intensity cross sections at the chip facet for $L_s = 1300$ and 5600 μm. Thick solid lines are simulation results of the first-order antisymmetrical resonance profile after propagating for the previously stated distances in a single-mode WG. The thin solid line is the simulated profile of the fundamental guided mode.

from the arc-to-straight WG interface (symbols). In the region proximal to the straight WG (located at $x = 0$), one can see that the distribution matches the WG's calculated fundamental mode profile (thin solid line). Outside of this region, it is seen that the distribution is fairly symmetrical and that it widens and flattens out as the distance from the arc-to-straight interface increases. Simulations of the first-order antisymmetrical leaky mode propagation in the straight single-mode WG (thick solid lines) match the measurements quite well. One can see that the arc-to-straight junction excites cladding modes, with the strongest contribution coming from the said resonance mode.

Multiple couplings between the cladding modes and the same WG at different localized points or between different WGs creates multiple paths for light propagation through the cladding and bound modes. Such strong multipath and multisource interference effects can lead to high sensitivity to polarization and wavelength. This detrimental phenomenon can be suppressed by minimizing the coupling between cladding and guided modes at the transitions between WGs of different curvature.

Manuscript received September 16, 2003; revised October 18, 2004.

The authors are with the Physics Department, The Technion—Israel Institute of Technology, Haifa 32000, Israel (e-mail: yoavbe@tx.technion.ac.il).

Digital Object Identifier 10.1109/JLT.2004.840006

In this paper, a simple design is presented for an adiabatic transition between WGs of different curvature—analyzed in detail is the case of transition between a straight WG and curved WG of constant radius that may be easily implemented in commercial integrated optics computer-aided design (CAD) packages. Experiments designed to evaluate the insertion loss, wavelength-dependent loss (WDL), and polarization-dependent loss (PDL) of the adiabatic transition design are described. Finally, the amount of radiation to the cladding modes for the no-offset, optimized offset, and adiabatic transition cases are experimentally compared.

II. Theoretical Background

The cause of loss at straight-to-curved single-mode WG junctions is the mismatch between the symmetrical shape of the straight section's bound mode and the asymmetrical shape of the curved section's leaky mode. It is assumed that the bending radius is large enough so that the radiative losses in the bend are small, and the leaky mode has a sufficiently long lifetime.

Using first-order perturbation theory, it is possible to expand the fundamental eigenmode of the curved section in terms of eigenmodes of the straight section. The leading correction is the first excited antisymmetric resonance term. It has been shown in [7] that a bent WG of curvature $\kappa = 1/R$ behaves like a straight WG with an effective refractive index given by

$$n^2_{\text{curve}}(x,y) = n^2(x,y)(1+2\kappa x) \tag{1}$$

where x is the transverse horizontal coordinate measured from the center of the WG, y is the transverse vertical coordinate, and $n(x,y)$ is the refractive-index profile of the WG and surrounding cladding, and we assume $|x| \ll 1/\kappa$. The index perturbation term $2n^2(x,y)\kappa x$ modifies the mode profile, with the most noticeable change being the lateral outward shift of the mode maximum. For bending radii with low radiation losses, this shift is inversely proportional to the bending radius [1], [2] and thus proportional to the curvature of the bend. Another effect is that the mode shape loses its symmetry with respect to the maximum.

The proposed design consists of inserting a WG section between the straight WG and the arc WG, where the local mode basis evolves from the symmetrical mode of the straight section to the asymmetric shifted mode of the arc section. In order to minimize the length of the transition section, the mode's lateral shift per unit length should be kept constant. This calls for a linear adiabatic increase in curvature so that the lateral shift of the mode linearly increases as the light propagates through the transition region. This requirement is graphically depicted in Fig. 2(a).

Let us describe the transition piece as the graph of a function $x(z)$ [see Fig. 2(b)]. We shall make the simplifying assumption that the transition is paraxial, i.e., it is almost parallel to the initial straight WG section and deviates from it only slightly so that $x'(z) \ll 1$. The local curvature $\kappa(z)$ of the paraxial transition piece is given by [8]

$$\kappa(z) = \frac{x''}{(1+x'^2)^{\frac{3}{2}}} \approx x''(z). \tag{2}$$

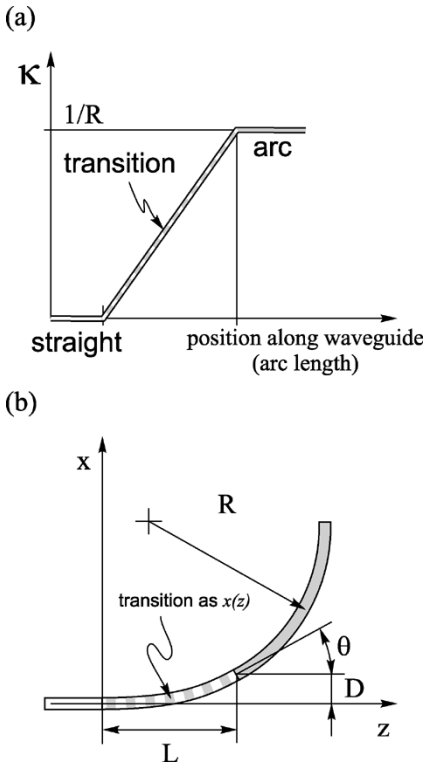

Fig. 2. Geometry of transition WG. (a) Ideally, the transition WG's curvature should change linearly with respect to the position along the WG from the straight WG's $\kappa = 0$ to the arc's $\kappa = 1/R$. (b) Geometrical layout of the transition piece (dashed) with respect to the straight section (white) and arc of radius R (gray). Under the paraxial approximation, the transition piece is described as a function $x(z)$. The parameter θ is the angle over which the transition occurs, L the length of the transition piece, and D the maximal lateral displacement of the transition.

The relative error in the curvature approximation of (2) is $\sim (3/2)(x'(z))^2$. For curves $x(z)$ where the deviation from the main axis z is less than 3°, the difference between the exact curvature and the approximation is less than 0.5%.

III. Design

Based on the previous section, the problem is formulated as a linear increase in the curvature of the transition section from the straight WG's $\kappa_{straight} = 0$ to the arc section's $\kappa_{arc} = 1/R$, all under the paraxial approximation. Fig. 2(b) describes the geometry of a general transition piece described as a function $x(z)$, where z is the paraxial propagation axis and x the lateral transverse axis. The transition piece is of length L in the z direction, with a lateral displacement D and an angle θ between the input and output.

Setting $z = 0$ at the beginning of the transition point, the linear increase in curvature is $\kappa(z) \propto z$. We assume the paraxial approximation and integrate using (2), yielding

$$x(z) = Az^3 \tag{3}$$

where A is a constant to be determined by the boundary conditions. Notice that lower powers of z are absent in the general cubic polynomial $Az^3 + A_2z^2 + A_1z + A_0$, resulting from

matching the beginning of the transition at $z = 0$ to the straight WG

$$\begin{array}{lcl} \text{No lateral offset} & \Rightarrow & A_0 = 0 \\ \text{Tangent-to-straight WG} & \Rightarrow & A_1 = 0\,. \\ \text{Zero initial curvature} & \Rightarrow & A_2 = 0 \end{array}$$

Matching to the arc at $z = L$ is formulated as the following conditions:

$$\begin{array}{lcl} \text{Displacement is } D & \Rightarrow & x(L) = D \\ \text{Tangent-to-arc WG} & \Rightarrow & x'(L) = \tan(\theta)\,. \\ \text{Arc's curvature} & \Rightarrow & x''(L) = \frac{1}{R} \end{array}$$

In fulfilling these conditions, there is a free parameter that can be chosen to be L or θ. If we choose θ as the free parameter, we obtain the following dependencies:

$$L = 2R\tan(\theta) \tag{4}$$

$$D = \frac{2}{3}R\tan^2(\theta) \tag{5}$$

$$A = \frac{1}{12R^2\tan(\theta)}. \tag{6}$$

For small θ, $\tan(\theta) \approx \theta$, and we see from (4) that the length L of the transition is approximately proportional to θ. Under the paraxial approximation, L also approximates the arc length of the transition piece. Therefore, the parameters L, θ are a measure of the transition's adiabaticity.

We performed scalar beam-propagation method (BPM) simulations to assess the transition loss from a straight section to an arc of 5000-μm radius for $\Delta n = 0.75\%$ 6×6 μm^2 rectangular WGs. The first set of simulations checked the dependence of transmission on the lateral offset at a straight-to-arc interface, and we found the optimal lateral offset to be 0.40 μm with a transition loss of 0.005 dB. This result is consistent with the fact that 100% overlap cannot be achieved by optimizing the offset as mentioned previously.

The second set of simulations checked the transition loss for the same straight and arc WGs, but with the cubic adiabatic transition section inserted in between them. The adiabaticity of transition section was varied by changing its length through the angle θ parameter. Fig. 3 shows the gain of the cubic transition over the offset-type transition at the optimal offset as a function of the transition angle θ. As we can see, the device reaches full adiabaticity for angles $\theta \geq 1.5^\circ$. This justifies the use of paraxial approximation. The gain relative to the optimal offset in the adiabatic regime is $\sim$0.004 dB, almost fully recovering the $\sim$0.005-dB loss of the optimal offset transition.

We would like to calculate the maximal curvature increase per unit arc length $(d\kappa/dL)_{\max}$ that preserves the adiabaticity of the transition. Let us assume that for a given radius R, the minimal angle for an adiabatic transition is $\theta_{\min}$. Since under the paraxial approximation, the curvature increase for the cubic transition is quasi-linear, we have

$$\frac{d\kappa}{dL} \approx \frac{\kappa_{\text{arc}}}{L} = \frac{1}{RL}.$$

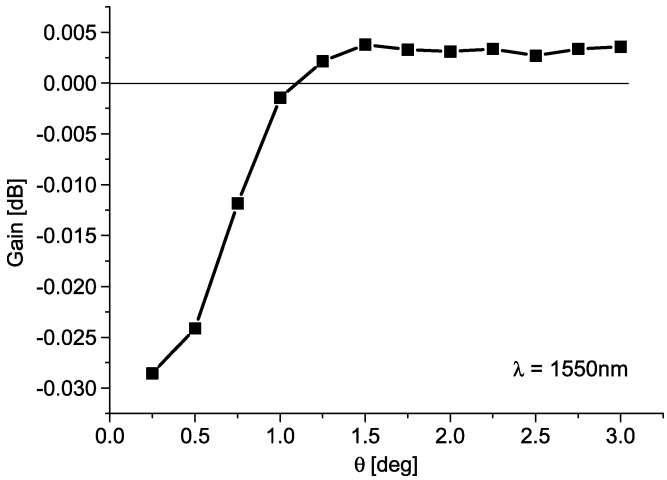

Fig. 3. Cubic transition simulations. Scalar BPM simulation results for the transmission between a straight WG and an arc of 5000-μm radius via a cubic transition piece. Gain relative to an optimal offset of 0.40 μm is plotted as a function of the cubic transition piece's angle θ.

Inserting L from (4) into this expression results in the following relationship between the minimal angle that allows an adiabatic trasition and the maximal curvature increase per unit arc length:

$$\left(\frac{d\kappa}{dL}\right)_{\max} = \frac{1}{2R^2\tan(\theta_{\min})}. \tag{7}$$

For example, in Fig. 3, we saw that the minimal angle for adiabatic behavior is $\theta_{\min} = 1.5^\circ$ in a transition to an arc of 5000-μm radius, giving $(d\kappa/dL)_{\max} \approx 7.5 \times 10^{-7}\,\mu\text{m}^{-2}$. This value can be used in (7) as a useful rule of thumb for finding $\theta_{\min}$ when scaling the cubic transition to different radii for WGs of similar composition.

From (4), we also see that the length of the transition segment is twice the length of a corresponding arc segment covering an angle θ at a radius R. This is the penalty paid in WG length and chip size for incorporating a smooth adiabatic transition compared with a lateral offset-type transition. As an example, for arcs of 5000-μm radius, a $\theta = 2.5^\circ$ cubic transition entails a WG length increase of 218.3 μm at each arc end. This length increase is a result of replacing the 218.3-μm-long, $\theta = 2.5^\circ$ arc section at each end with the corresponding cubic transition, which is 436.6 μm long.

IV. Samples and Experiment

The design was implemented in a silica-on-silicon planar lightwave circuit (PLC). Rectangular WGs were fabricated in a plasma-enhanced chemical-vapor deposition (PECVD) process with a germanium-doped core of 6-μm height and $\Delta n = 0.75\%$ index contrast. The single-mode WGs have a rectangular 6×6 μm^2 cross section. We implemented two experiments on two samples: the first designed to check insertion loss as a function of the transition angle θ and the second to measure the radiation of transition loss into the cladding for various transition designs.

The experimental setup consisted of a continuous-wave external-cavity tunable fiber-coupled laser, a deterministic polarization controller, a bare-end fiber on an alignment stage to

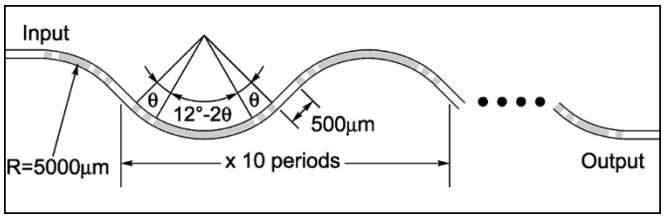

Fig. 4. Sample 1: Cubic transition loss characteristics experiment. Schematic layout for single test device, which consists of ten concatenated S-bend periods. Straight sections are white, cubic transitions are dashed, and arc sections are gray.

couple the light into the chip, and another bare-end fiber for coupling the light out of the chip and into a detector. The laser wavelength range was 1510–1640 nm, the optical power was 3 dBm (2 mW) for single-wavelength measurements, and −4.5 dBm (0.3 mW) for swept-wavelength measurements. The polarization controller was used for four-state measurement following the Mueller matrix method [9], yielding average transmission and PDL at the same measurement. For measuring radiation in the cladding, we used unpolarized light, scrambled at the laser output, and laterally scanned the output facet with a bare fiber. Measurements were performed at room temperature, with the chip temperature stabilized at 24 °C.

The sample layout for the first experiment is schematically depicted in Fig. 4 (we will refer to this sample as sample 1). Due to the expected low loss per transition, each test device has ten concatenated S-shaped periods, where each period consists of alternating left-curving and right-curving half-period sections. Each half-period has a straight section, 500 μm long (white), a cubic transition of angle θ (dashed), an arc of $R = 5000$ μm extended over an angle of $12^\circ - 2\theta$ (gray), and finally another cubic transition with an angle θ so that each half-period covers a total 12° change in the WG direction, regardless of the transition angle θ. We shall term the cubic–arc–cubic structure a "smoothed arc." Coupling to the input/output facets is done via smoothed-arc sections similar to the half-periods, but with a total angle of 6°. The total number of cubic transition sections in the device is therefore 44. The sample itself contains 13 such devices, each one with a different transition angle, covering the range of $\theta = 0^\circ$ to 3°, in increments of 0.25°. In addition, straight single-mode WGs of the same profile were placed in parallel and in close proximity to the test devices for reference purposes.

The second sample (sample 2) contains test devices to check the radiation of transition losses into the cladding. Since the signals expected at the output facet were very weak, the general WG configuration is U-shaped,[1] as depicted in Fig. 5. The sample contains devices with cubic transitions of 2.5° and devices with offsets of 0.40 μm. We chose a cubic transition angle of 2.5° to make sure the device is well into the adiabatic regime, and an offset of 0.40 μm, which has the least insertion loss (based on previous experiments and simulations). Each type of device was repeated five times to check uniformity and consistency. The U shape was divided into four 45° curved sections with intermediate straight WGs of varying length, enabling all arcs to have a constant radius of 5000 μm, and keeping the distance between the input (output) facet and the first (last) transition constant at 5000 μm.

[1]By using the U-shaped chip configuration, the uncoupled light of the input fiber does not reach the output facet, and we measured (at the output facet) a background in the order of -90 dB, limited by the detector SNR.

V. Results

A. Sample 1

In Fig. 6, we show the insertion loss of the cubic transition concatenated S-bend devices as a function of the transition angle θ at a wavelength of 1550 nm. The symbols are the measured transmission, while the solid line represents the simulation results already shown in Fig. 3, normalized to the 44 transitions in each device and to the fiber-chip coupling loss (FCC $= -1$ dB as measured on reference WGs). We find good agreement between experimental results and simulations in the adiabatic region ($\theta \geq 1.5^\circ$), yet at small angles the actual loss is higher than expected.

Next, a wavelength sweep from 1510 to 1640 nm was performed on the same devices. The PDL was calculated at each wavelength by the Mueller matrix method, as was the transmission average over all polarizations. The transmission was then normalized to the reference WG transmission to yield the net transmission for the device (the inset of Fig. 7). The main plot in Fig. 7 presents the maximal PDL value and the maximal variation in net transmission (wavelength-dependent loss, or WDL) over the above spectral range.

We find that for all angles $\theta \geq 1.5^\circ$, the transmission at 1550 nm is constant, and the WDL and PDL are very small and independent of θ. This indicates that the device is truly adiabatic for angles $\theta \geq 1.5^\circ$, just as the simulations predict. For these angles, we relate the nonzero PDL and WDL mainly to the bending losses in the $R = 5000$-μm arcs. For smaller angles, the transmission at 1550 nm decreases (Fig. 6), and the WDL and PDL increase considerably (Fig. 7).

Now, we can explain the discrepancy between the simulation and the measured transmission of Fig. 6. The simulation was performed for a single transition and multiplied by the number of transitions, whereas the actual device contains 44 concatenated transitions. Therefore, transitions with small angles (which have higher loss) couple strongly to the radiating cladding modes, and the device is subject to interference effects from 44 such couplers. This was not taken into consideration in the simulations. These interference effects also explain the increased WDL and PDL for small transition angles. The inset in Fig. 7 displays this effect. Note the strong wavelength-dependent behavior of the net transmission and PDL for $\theta = 1^\circ$, a clear indication of multipath interference. This is in contrast to the results for $\theta = 2^\circ$, where we find very low wavelength-dependent transmission variations and PDL.

B. Sample 2

Fig. 8 shows intensity distribution cross sections at the output facet for the cubic transition (thick solid line) and the offset transition (thin solid line) U-turn WGs. The intensity was normalized to 0-dB transmission at the peak. The results are for a single device of each type; the others show similar results. The central peak corresponds to light in the fundamental mode of the final

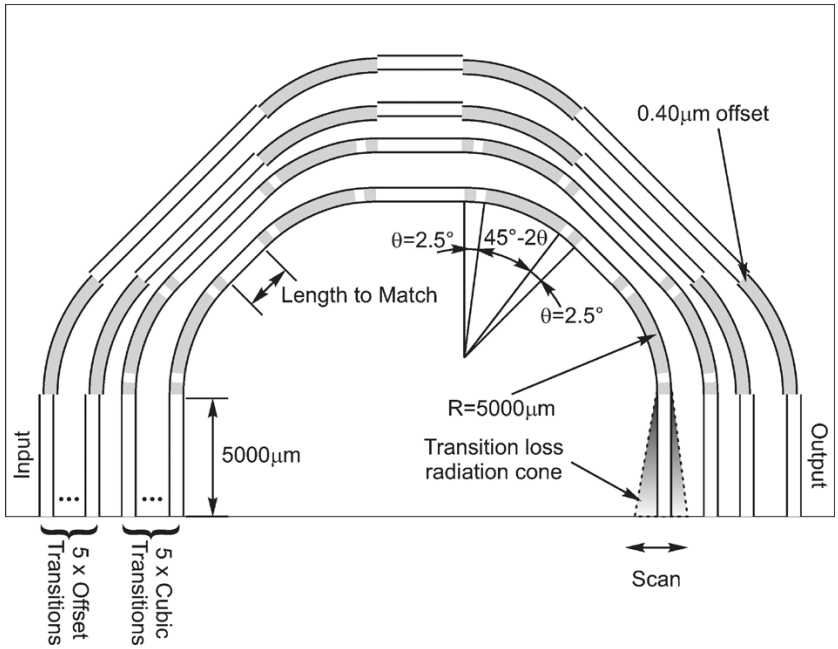

Fig. 5. Sample 2: Transition loss radiation to cladding experiment. Schematic layout for a series of ten test devices. Straight sections are white, cubic transitions are dashed, and arc sections are gray. The inner five devices have cubic transition segments of $\theta = 2.5°$, and the outer five devices have offset type transitions of 0.40 μm. Note that the 90° bends have been split into two sections to enable a constant arc radius of 5000 μm and constant distance of 5000 μm from the final transition to the output facet for all devices.

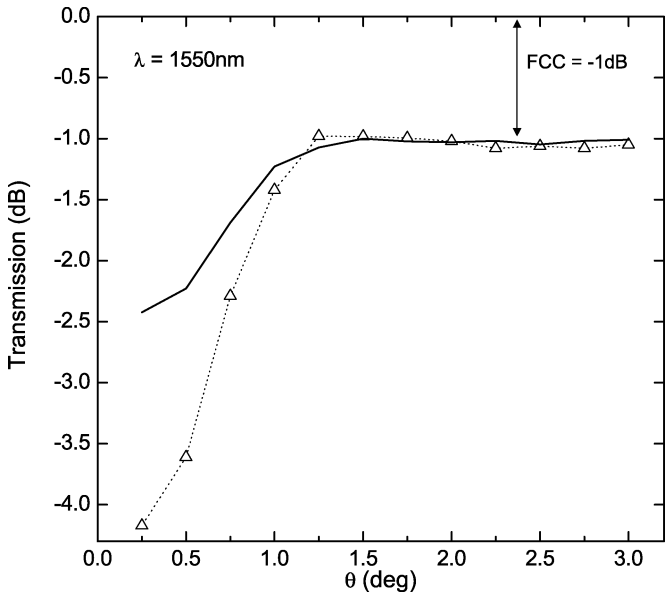

Fig. 6. Sample 1: Insertion loss in cubic transition S-bend devices as a function of the angle θ. Measured transmission (symbols) and normalized scalar BPM simulations (solid line) at a wavelength of 1550 nm.

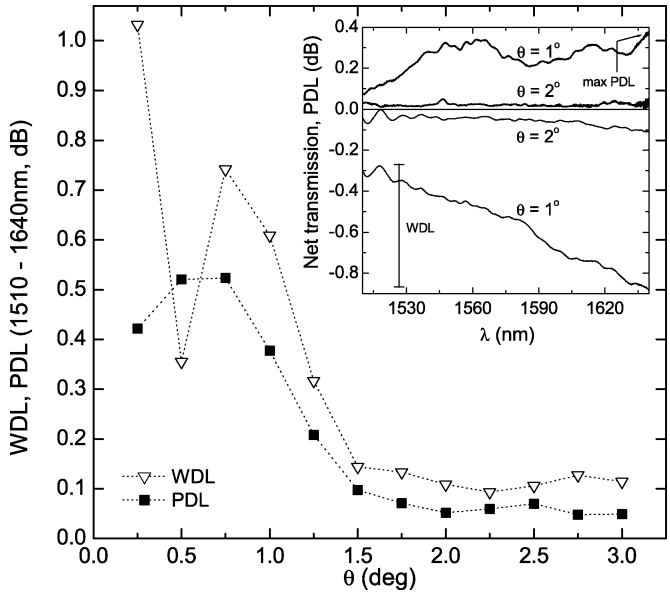

Fig. 7. Sample 1: Maximal WDL and PDL in the spectral range of 1510–1640 nm as a function of the transition angle θ. Inset: PDL and net transmission as a function of wavelength for two devices with transition angles $\theta = 1°, 2°$.

straight single-mode WG. The side lobes consist of radiating mode contributions from the different loss mechanisms in the device, mainly arc bending loss, transition loss, and process-induced WG propagation loss.

From simulations and measurements of concatenated S-bend structures (similar to those of sample 1), we find that the transition loss is in the order of $\sim 0.003 \pm 0.002$ dB per transition (for both the 0.40-μm offset and the $\theta = 2.5°$ cubic transition). We have measured bending losses of $\sim 5 \times 10^{-4}$ dB/degree for arcs of 5000-μm radius, and propagation loss in straight single-mode WGs of 0.013 dB/cm. These figures indicate that bending losses over the last few degrees and propagation losses along the 5-mm straight WG section are of the same order as the transition loss at the final arc-to-straight interface. All three loss mechanisms contribute to the low-intensity side lobes in Fig. 8 at comparable levels. The slight asymmetry of the side lobes, with stronger intensity on the outer side of the bend matches the pattern we expect from bending losses.

Compared with the offset transition, we find that the side lobes of the cubic transition are lower by 5 to 10 dB, and the

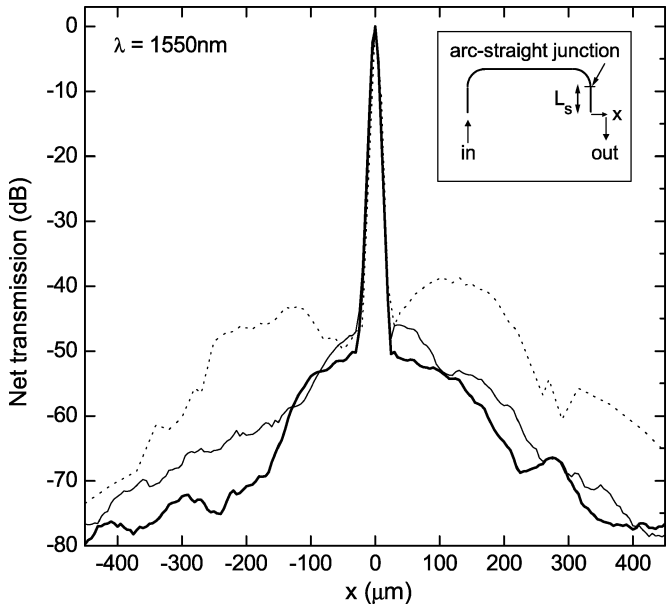

Fig. 8. Sample 2: Intensity distribution cross section at the output facet; 5000 μm after the final arc-straight WG transition. Results are shown for a typical cubic transition device (thick solid line) and a typical offset transition device (thin solid line). The intensity distribution cross section at $L_s = 5600\ \mu$m from Fig. 1 (dashed line) is added for comparison.

overall integrated intensity is smaller by 50%. This indicates that the cubic transition has much weaker coupling to the radiating modes. This measurement is therefore much more sensitive than a direct measurement of insertion loss as quoted previously. Finally, compared with no offset at the arc-straight WG junction (dashed line in Fig. 8), the introduction of an optimized offset or an adiabatic cubic transition segment dramatically decreases the excitation of radiation modes.

VI. Summary

We have designed an adiabatic transition between straight and curved WGs, based on a cubic polynomial. The design is very simple, easy to optimize, and has low insertion loss, WDL, and PDL. Moreover, high transition losses, which could lead to erratic polarization and wavelength dependence due to multipath interference between the WG's bound and radiating modes are suppressed by the smooth adiabatic transition. Measurements of radiation in the cladding indicates that the cubic transition has smaller coupling to the cladding modes than traditional offset-type transitions, even though both have the same measured insertion loss. Such measurements of the radiation in the cladding provide a tool for evaluating transition designs that are indiscernable with respect to their measured insertion loss. Further empirical tuning of the offset transition might lower the radiating side lobes, but this will be very sensitive to the offset dimension and process parameters [5] and cannot be optimized by measuring the device's insertion loss (within the measurement error). Moreover, from the theoretical point of view, the offset transition can never reach 100% overlap, while the adiabatic transition can.

Acknowledgment

The authors would like to thank S. Aharon, A. Meller, and R. S. I. Segal for their assistance in optical measurements.

References

[1] V. Subramaniam, G. N. De Brabander, D. H. Naghski, and J. T. Boyd, "Measurement of mode field profiles and bending and tranistion losses in curved optical channel waveguides," *J. Lightw. Technol.*, vol. 15, no. 6, pp. 990–997, Jun. 1997.

[2] T. Kitoh, N. Takato, M. Yasu, and M. Kawachi, "Bending loss reduction in silica-based waveguides using lateral offsets," *J. Lightw. Technol.*, vol. 13, no. 4, pp. 555–562, Apr. 1995.

[3] W. Minford, S. Korotky, and R. Alferness, "Low-loss Ti:LiNbO3 waveguide bends at $\lambda = 1.3\ \mu$m," *IEEE J. Quantum Electron.*, vol. 18, no. 10, pp. 1802–1806, Oct. 1982.

[4] F. Ladoucer and P. Labeye, "A new general approach to optical waveguide path design," *J. Lightw. Technol.*, vol. 13, no. 3, pp. 481–492, Mar. 1995.

[5] M. Heinbach, M. Schienle, A. Schmid, B. Acklin, and G. Müller, "Low-loss bent connections for optical switches," *J. Lightw. Technol.*, vol. 15, no. 5, pp. 833–837, May 1997.

[6] D. Marcuse, *Theory of Dielectric Optical Waveguides*. New York: Academic, 1974.

[7] A. W. Snyder and J. D. Love, *Optical Waveguide Theory*. London, U.K.: Chapman & Hall, 1984.

[8] M. P. do Carmo, *Differential Geometry of Curves and Surfaces*. Englewood Cliffs, NJ: Prentice-Hall, 1976.

[9] D. Derickson, Ed., *Fiber Optic Test and Measurement*. Englewood Cliffs, NJ: Prentice-Hall, 1998.

Yoav Berlatzky, photograph and biography not available at the time of publication.

Itay Shtrichman, photograph and biography not available at the time of publication.

Romanas Narevich, photograph and biography not available at the time of publication.

Edvardas Narevicius, photograph and biography not available at the time of publication.

Gershon Rosenblum, photograph and biography not available at the time of publication.

Ilya Vorobeichik, photograph and biography not available at the time of publication.